https://doi.org/10.1038/s44182-026-00078-z

Harnessing proprioception in aquatic soft wings enables hybrid passive-active disturbance rejection

Leo Micklem[1], Huazhi Dong[2], Francesco Giorgio-Serchi[2] ✉, Yunjie Yang[2], Blair Thornton[1,3] & Gabriel D. Weymouth[4]

Soft robotics offers a venue to narrow the gap in manoeuvrability and efficiency between engineered vehicles and swimming or flying animals. Yet, state estimation and control of highly deformable structures remain challenging, leaving soft robots vulnerable to unsteady environmental flow disturbances. Inspired by animals' ability to sense and respond to fluid forces via appendage shape changes, we demonstrate a soft robotic wing with a flexible proprioceptive e-skin that autonomously detects and compensates for sudden disturbances. Experiments show that while the wing's passive elastic compliance alone mitigates lift deviation compared to a rigid wing, it still leaves a large unwanted lift bias. By integrating proprioception and active shape morphing, we establish a hybrid passive-active disturbance rejection strategy in which passive material compliance reduces baseline deviations and active control suppresses residual biases. This combination autonomously reduces the unwanted lift impulse over the disturbance by 87%, closely matching the gust-rejection abilities of some flying animals. These results demonstrate how embodied intelligence and hybrid control could naturally endow soft robots with disturbance-resilient capabilities akin to those of living organisms.

In nature, plants and animals have inherently flexible and deformable bodies. This allows them to easily alter their body shape to reduce the effects of external disturbances[1,2]. For example, deformations which optimise the lift-to-drag ratio have been found to offset structural failure and hence facilitate survival in plant leaves subject to increasing wind speeds by maintaining low drag[3]. In avian flight and sea dwelling organisms, the need to cope with flow disturbances is mediated by a combination of active and passive alteration of the foils, be it birds' wings or fish fins, Fig. 1. Active disturbance rejection in birds and fish relies on precise proprioceptive and exteroceptive stimuli: in the birds feathers, mechanoreceptors which are sensitive to strain and vibrations provide information on fast changing flow conditions[4,5] thus enabling certain specimen to perform remarkable feats such as the stationary hovering of kestrels[6] and the gust rejection during glide of the barn owl[7]. In fish, highly unsteady fluid loading are sensed via a combination of the neuromasts within the *lateral line*[8] and the proprioceptive inputs from the fin rays[9], Fig. 1, resulting in the outstanding swimming performances of certain specimen such as the *Karman gaiting* of trouts[10,11] and the fin-based manoeuvreing of the bluegill sunfish and the parrotfish[12].

There is strong evidence that biological systems make use of shape feedback for unsteady fluid load estimation and control[13–16]. In self-propelling organisms, this results in significantly higher manoeuvrability for equivalent efficiency compared to engineered rigid autonomous vehicles[17–22]. Indeed, a major factor for the loss of efficiency of self-propelled vehicles, when undertaking highly unsteady manoeuvres is, on one hand, their limited flow sensing capabilities and, on the other hand, their rigid nature. At best, man-made self-propelled systems are streamlined in one direction, implying that motion in any other direction will be subjected to large drag and added mass forces that must be overcome. This is relevant for aerial vehicles, but even more so for autonomous underwater vehicles (AUVs) or other aquatic robots which must contend with a highly turbulent, dense medium.

In the oceans, disturbances from currents and waves manifest themselves through fast changes in direction and speed of the flow, making collision avoidance and path following tasks often difficult to achieve for AUVs[23]. This effectively prevents any close-quarter operation or contact-based tasks outwith perfectly unperturbed environmental conditions. In addition, the effects of disturbances must be accounted for with high-energy motor inputs and often highly aggressive control[24], making disturbance rejection a costly endeavour.

An area of potential inspiration from nature for managing varying fluid loading is the design of morphing wings. Both in aerial and aquatic

[1]Department of Civil, Maritime, and Environmental Engineering, University of Southampton, Southampton, UK. [2]School of Engineering, University of Edinburgh, King's Building Campus, Edinburgh, UK. [3]Institute of Industrial Science, The University of Tokyo, Bunkyo City, Tokyo, Japan. [4]Faculty of Mechanical Engineering, Delft University of Technology, Delft, Netherlands. ✉e-mail: f.giorgio-serchi@ed.ac.uk

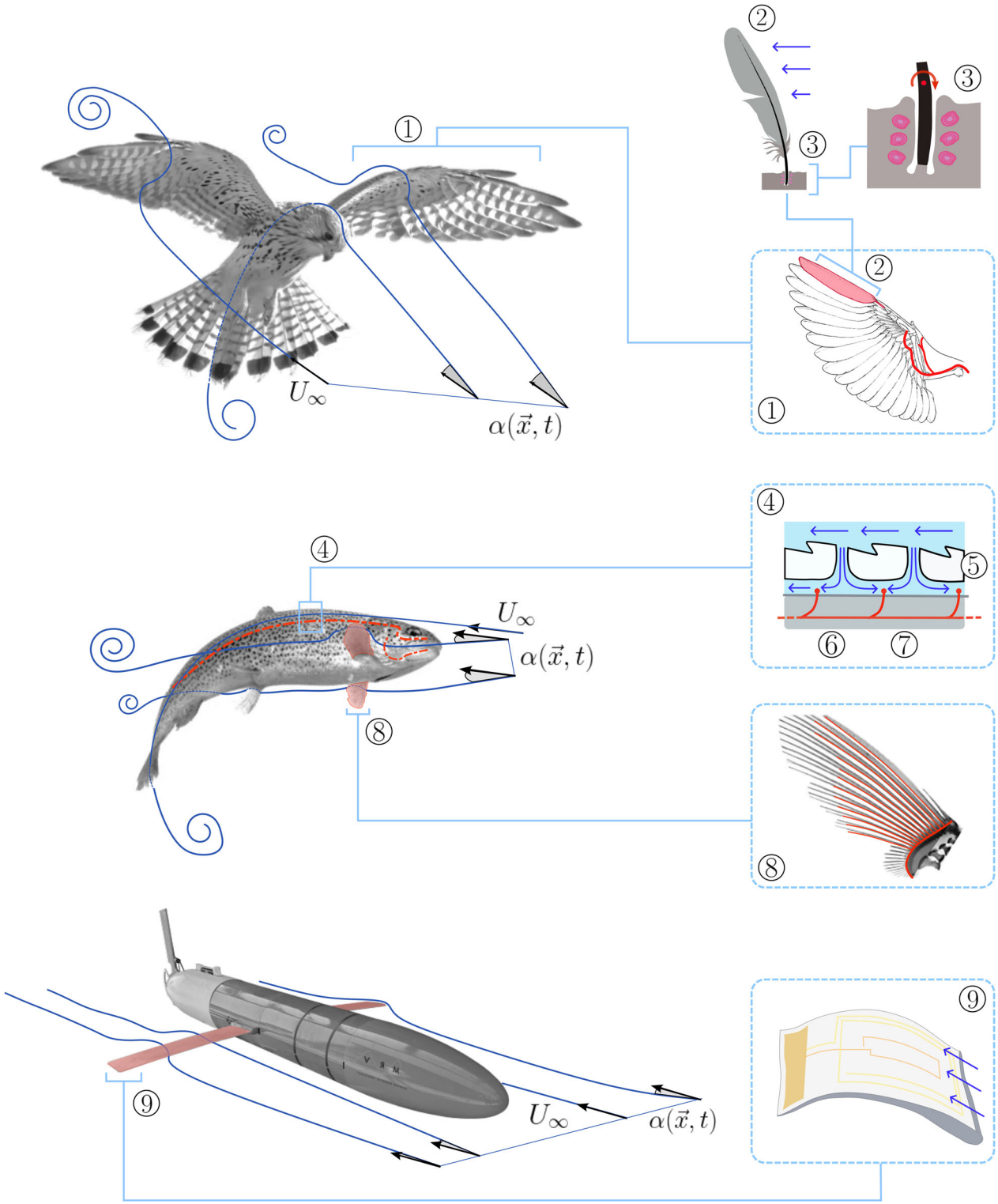

Fig. 1 | Biological and biologically-inspired, proprioceptive, disturbance rejecting wing. Animals are able to maintain station or trajectory in the presence of disturbances, represented here by an ambient flow of mean speed U_∞ approaching the body with an angle of attack $\alpha(\vec{x}, t)$ which may vary in space and time. Birds' wing (1), sense flow variations through the feathers' (2) strain and vibration thanks to dedicated mechanoreceptors (3), thus ensuring a fast feedback loop with the wings' muscles. Fish sense the flow state via the *lateral line* (4), where penetration of the fluid through the epidermis (5) excites neuromasts (6) connected to the nerves; they also exploit innervated fin rays (8) to perceive local flow-induced loads. Excitation of the appendages exposed to the flow allows animals to proprioceptively change shape and spontaneously cope with disturbances. This principle is used here to design a proprioceptive engineered morphing wing (9) which detects the onset of flow variations thanks to abrupt shape changes of the wing, thus enabling fast mitigation of the disturbance.

propulsion, foils are widely used as control surfaces for trajectory following, stability and thrust generation[25,26].However, rigid foils can only be fully optimised for a relatively narrow range of flow conditions and their stiffness may be detrimental to stability in highly unsteady fluid loading.

On the other hand, wings that are morphologically adaptable, either passively or actively, may allow for the wing to conform to an optimal shape according to the instantaneous flow state, providing improved flight stability, reduced noise and drag[27]. This result is of little surprise when birds are observed, twisting and turning effortlessly in the air with their highly adaptable wings[7,28]. The benefits associated with morphing wings have led to much research in this area, with several examples of morphing wing prototypes documented in refs. 29–33. Typically, morphing wings consist of linkages with some compliant, flexible unit to allow for relative displacement[29,31]. While these methods successfully allow for shape change and control of the wing, they are limited in terms of range of motion and response time. For example, the shape memory alloy (SMA) wing in ref. 31 has a response time of 17 s for a wing tip angle change of 8°, and the one in ref. 29 has a maximum deflection of 19 mm over a 600 mm chord. Although highly adaptable, man-made morphing airfoils suffer from limited range of motion, high energy requirement and poor responsiveness to external disturbance compared to their biological counterpart.

Soft robotics offers an avenue to bridge the gap between traditionally engineered foils and biological ones[34]. This is because the structural flexibility and continuous nature of soft devices lend themselves to fine-tuning of the unsteady fluid loading with benefits on sustained flying and swimming efficiency as well as agile manoeuvreing[35]. Importantly, the deformability of the structure naturally represents a potent clue in the interpretation of external forces if complemented by suitable proprioceptive systems, similarly to what is observed in the appendages of birds and fish[5,9], Fig. 1.

Soft morphing wings have been studied extensively[36] as representative biomimetic model for fish propulsion[37] and for potentially offering a versatile option for underwater vehicle manoeuvreing and prolusion[38]. As an example, fish capability to tune tail flexibility through muscle contraction for optimal propulsive efficiency has been successfully replicated via flexible foils with variable stiffness actuators[13,39]. However, in order to harness the full potential of bioinspired soft foils as tools for accurate flow control[40], ad hoc soft proprioceptive systems are essential[41]. Large nonlinear deformations and application in fluid environments represent key limiting factors in the design of sensing devices for soft systems[42–44]. While still in its infancy, e-skin technology in combination with machine learning has shown great promise in closing the control loop of soft robots, especially for systems with fewer degrees of freedom[45–47]. More recent developments in e-skins allow for point cloud-resolution shape reconstruction[48], potentially endowing soft robots with the ability to better interact with the environment[49]. Despite significant advancements[50–52], current sensing technologies lack adequate solutions to the challenge of accurate state estimation which is required to achieve the fine control necessary for underwater manoeuvrability and disturbance rejection in realistic, non-stationary flow conditions[43,53]. This is particularly true in underwater applications and may represent one of the major impediments to the adoption of self-propelling underwater soft robots in real-world environments.

Taking the cue from the study of avian and fish strategy to disturbance rejection, we develop a soft proprioceptive wing that leverages its own subtle deformations captured by an integrated e-skin to detect impending flow variations and quickly respond to these by modifying its own shape, thus minimising unwanted fluid loadings. The combined disturbance detection and rejection capability inherent to the soft nature of the wing is a powerful example of embodied intelligence in the context of flow control[54–56]. In particular, the integration of passive material compliance with active proprioceptive control highlights a hybrid passive-active strategy, underscoring how simplistic control approaches can achieve robust navigation in highly perturbed fluid environments.

The proprioceptive wing developed in this work (Fig. 2C) integrates a newly designed e-skin with a highly deformable soft wing structure. Building upon the mechanical platform of ref. 57, we introduce a novel capacitive e-skin architecture adapted for underwater proprioception. While our e-skin design builds upon the previous platform presented in ref. 48, the present work introduces key innovations and adaptations to enhance sensing performance, better fit the soft wing and address the challenges of underwater deployment. These challenges include the need to be water-tight, the attenuation of signals underwater, and the comparatively harsh environmental conditions. The central advancement lies in the adoption of a line-shaped electrode topology. While both architectures can theoretically function underwater, the previous design relied on carbon black-silicone electrodes, which possess lower conductivity and necessitate specific spacing between electrodes. This spacing precluded dense layouts, limiting the resolution of deformation sensing. In contrast, the current work adopts liquid metal-based line-shaped electrodes. This topology provides significantly higher conductivity and allows electrodes to be placed more densely and uniformly, enabling the capture of finer deformations and subtle shape changes required for detecting fluid disturbances. Strategic placement of longer electrodes in regions of higher curvature amplifies the potential gradient response, resulting in more accurate mapping of distributed curvature along the soft robotic body. Finally, the move to line-shaped liquid metal electrodes eliminates the complex multi-layer fabrication procedures inherent to the previous carbon black design, resulting in a simplified fabrication process and a more robust integration better suited for the rigors of underwater operation. Details on the mechanical fabrication, characterisation and sensor training protocols are provided in Methods.

Appropriate training, as reported in Methods, allows interpretation of the instantaneous readout from the e-skin as a continuous sequence of states in the curvature of the foil, Fig. 2B. This allows for accurate proprioception in estimating the state of the flexible underwater wing without the use of an external measurement system that might disrupt the body's flexibility and that allows for use outside of a lab setting. Upon training, the flexible e-skin is able to track the centre line of a submerged rapidly morphing soft robotic wing section, as defined in Fig. 3C, allowing for the wing camber to be treated as the control variable and thus enabling camber setpoint regulation as shown schematically in Fig. 6a. When not subject to external flow disturbances, the accuracy of the state estimation and closed-loop camber control is, on average, within 0.52% of ground truth with a maximum error of 2.2% within the calibrated range (which corresponds to a 0.5–40 mm wing tip deflection range). Full details are reported in Methods, see Figs. 13, 14.

The apparatus shown in Fig. 3A allows to mimic the onset of a sudden change in flow direction, i.e., a gust, by allowing for abrupt yaw rotation of the wing. By employing camber observation alone, we demonstrate the automatic detection and rejection of the gust, as schematically depicted in Fig. 4. Here, the gust is represented by a sudden change in angle of attack relative to the oncoming flow. This triggers a sudden deviation of the lift force on the wing, which generates a change in camber due to the soft nature of the foil. To identify the onset of the gust, the controller monitors the camber via the e-skin and looks for a sudden excitation of the camber profile, immediately followed by its decaying oscillations, Fig. 4, similarly to what happens in living organisms[7]. The detection of the initial overshoot in camber response, see Fig. 4, can be exploited to trigger the disturbance detection and controller's response, thus ensuring a faster reaction. Following this, Fig. 3B outlines the planned experimental tests. The top section shows the scheduled disturbances in the form of a sudden change in angle of attack. The system is tested against a triangle wave and a square wave gust of various magnitudes. Minimisation of the lift force deviation on the foil as a result of change in angle of attack provides a metric to assess the effectiveness of the autonomous disturbance detection and rejection. The non-controlled case, which has no active change in camber (middle section in Fig. 3B), will exhibit a large deviation in lift coefficient corresponding to the profile of the disturbance, as schematically shown in the bottom section of Fig. 3B. An ideal controlled case, instead, should adjust the camber perfectly to the disturbance to completely mitigate any change in lift force, bottom section of Fig. 3B.

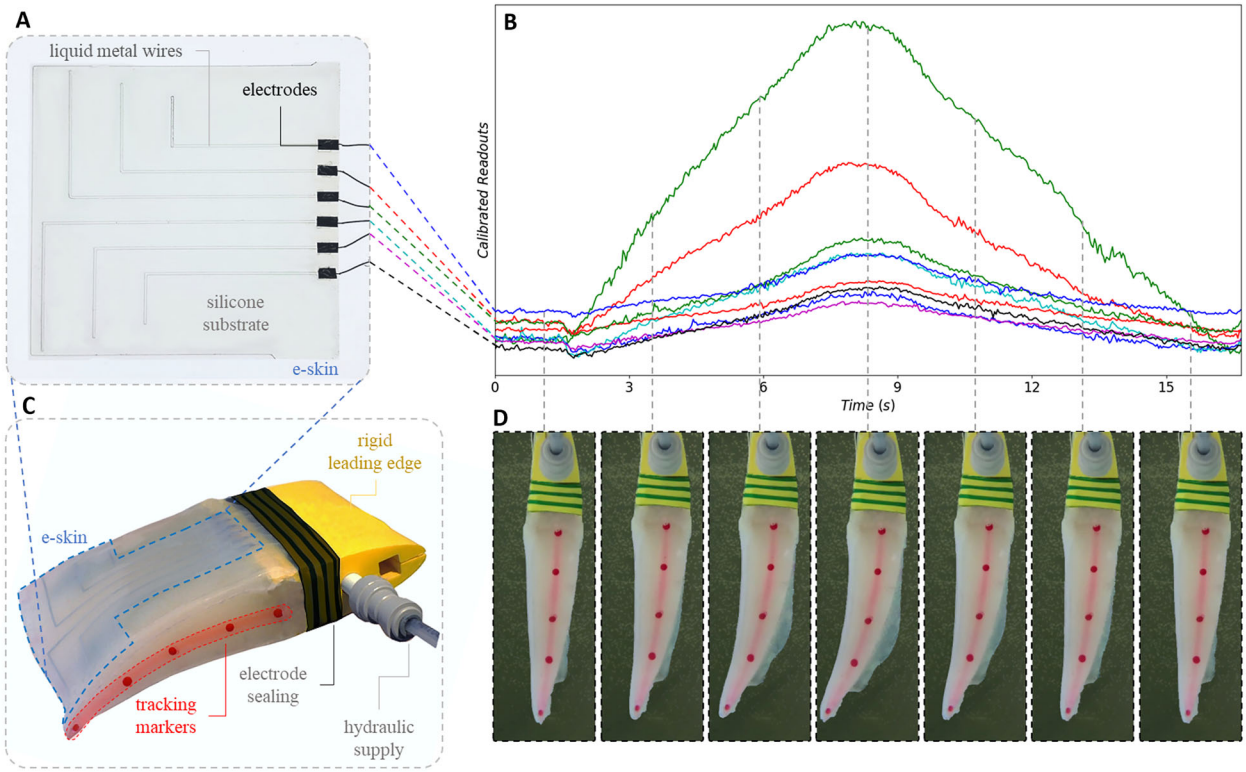

Fig. 2 | Proprioceptive wing schematic with e-skin training. A the e-skin structure showing the thin silicone layer with 6 liquid-metal wires which allow for the reading of nine capacitance signals (**B**) for training and state estimation. In **B**, the curves of calibrated capacitance readouts are shown during experiments: each readout is calibrated as follows: $c = (c' - c_o)/c_o$, where c is the calibrated capacitance readout, c' is the original readout, and c_o is the readout without deformation. **C** The soft robotic foil with highlighted: the e-skin, tracking markers for underwater training and ground truth comparison and the hydraulic supply for the hydraulic actuators enclosed within the foil (not shown). **D** The corresponding foil deformation to the readouts over one actuation cycle.

Results

Disturbance Mitigation Via Camber Control

We start by examining the capability of an actuated soft wing to mitigate prescribed disturbances by means of camber variation. To do this, the experimental set up of Fig. 3A, B is employed in a static configuration, where the soft foil is subject to flow at different angles of attack (namely from -15° to +15° at 5° intervals) for different camber configurations (namely 3, 3.5, 5, and 6.5%). The results, presented in Fig. 5A, show the static lift coefficient plotted against angle of attack for the four values of camber, averaged over three trials. The inserted images depict the camber and angle of attack for 3% and 6.5% camber at 0° and 15° angle of attack. Due to the camber of the wing section, even at the most flexible condition, there is a non-zero lift coefficient at 0°. This plot shows that different lift coefficients are achievable by the same wing section at the same angle of attack by adjusting the camber. More pertinent to this study, the same lift coefficient is achievable at different angles of attack by adjusting the camber, as indicated by the dashed green line. This demonstrates that deviation from a reference lift can be actively mitigated by exerting authority over the wing camber.

We later subject the soft wing to a dynamic change in angle of attack and scheduled an open-loop response of the soft actuator so as to minimise the lift deviation associated with the gust. This idealised open-loop case, in which the disturbance onset is known a priori, serves as a benchmark to illustrate the system's theoretical potential and to provide a reference for the subsequent non-prescient evaluation. The results are shown in Fig. 5B, C where Fig. 5B plots the disturbance input, the internal pressure of the actuator, and lift coefficient deviation for non-controlled and open-loop controlled test cases, averaged over five trials. The data is plotted against convective cycles, tU/L (in this case one convective cycle is equal to one second). The green dashed line in the top section of Fig. 5B shows a triangle wave disturbance from 15° to 5° over 20 s. The middle section shows non-dimensionalised internal pressure coefficient for the internal stiffening tubes, where an increase in pressure results in an increase in camber. The non-controlled baseline, in blue, has no change in pressure, whereas the open-loop controlled case, in red, increases and decreases pressure inversely to the disturbance. The systems' response to the gust is shown in the bottom section of Fig. 5B, where the lift coefficient deviation is plotted. An ideal case would have zero lift deviation, thus completely mitigating the disturbance, as postulated in Fig. 3B. The open-loop control case almost achieves this, reducing the impact from a 50% decrease in the lift coefficient to a 10% decrease.

Figure 5C summarises the maximum lift coefficient deviation for all triangle wave disturbances using a violin plot. The red violins are the open-loop controlled cases with varying pressure profiles. The blue violins are the non-controlled cases. The black points correspond to the theoretical quasi-static lift coefficient deviation achieved by extrapolating from the static measurement points in part (A) of Fig. 5. The non-controlled cases suffer from a larger disturbance than the theoretical quasi-static prediction due to the dynamics of the motion.

Having demonstrated the possibility to mitigate gust effects in an open-loop mode, we now move onto the fully autonomous disturbance detection and rejection.

Hybrid Passive-Active Disturbance Detection and Rejection

For the objective of hybrid passive-active disturbance detection and rejection, the fully actuated soft wing equipped with proprioceptive e-skin is used, Fig. 2A, as part of the control strategy schematically depicted in Fig. 6b. The e-skin allows for real-time camber estimation, feeding the controller with a means to identify the onset of a gust; the controller can therefore respond to minimise the camber deviation using a proportional controller which commands the internal hydraulic actuators. We employ a control

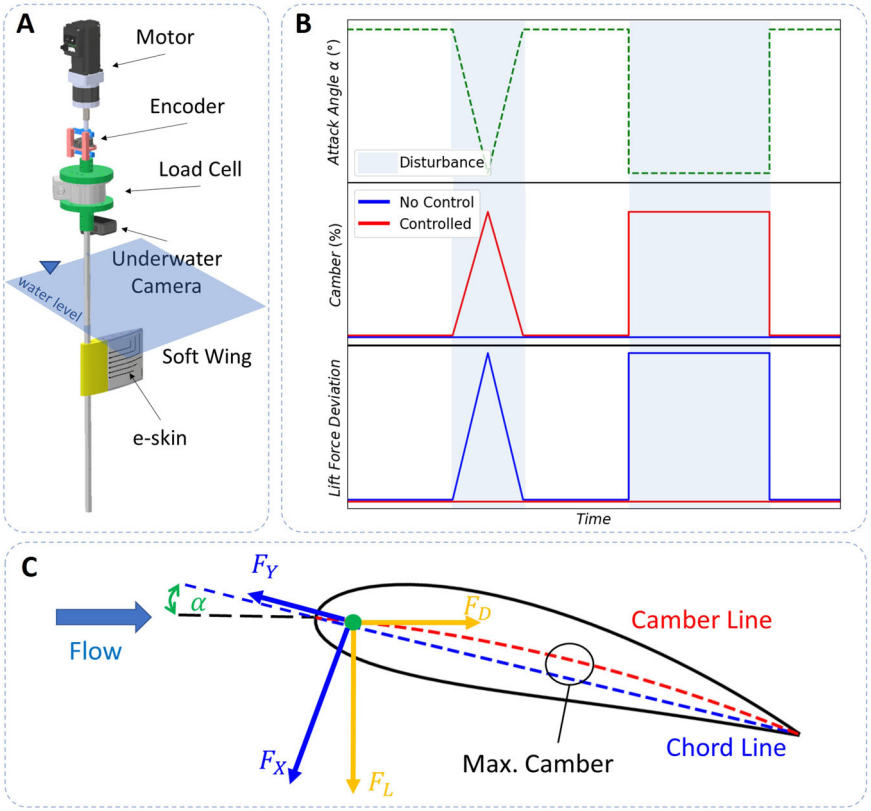

Fig. 3 | Experiment schematics. A Schematic of the static testing set up. The wing section is mounted in a recirculating Water Tunnel 1.5 chord lengths from the tunnel floor and from the surface plates above. The motion of the wing is controlled by a stepper motor with motion measured via an encoder. Forces are recorded with a 6-axis ATI load cell. The pressurisation of the wing is controlled using an Arduino Uno and Cytron MD10C Motor Driver. A linear actuator connected to a syringe supplies the pressure. **B** Experiment plan: the green line shows the disturbances in the form of an angle of attack change. The *No Control* case has no active camber change which results in a large lift force deviation as an effect of the disturbance. The ideal *Controlled* case adjusts the camber perfectly to the disturbance, mitigating any change in lift force. **C** Outline of the key physical parameters for the control problem. The angle between any oncoming flow and the leading edge α is the angle of attack. The straight line from the leading edge to the trailing edge is the chord line. The line from leading edge to the trailing edge through the centre of the foil is the camber line. The perpendicular distance between the chord and the camber lines gives the camber. The forces are measured in the local coordinate system F_x, F_y and transposed to the streamwise coordinate system F_L, F_D.

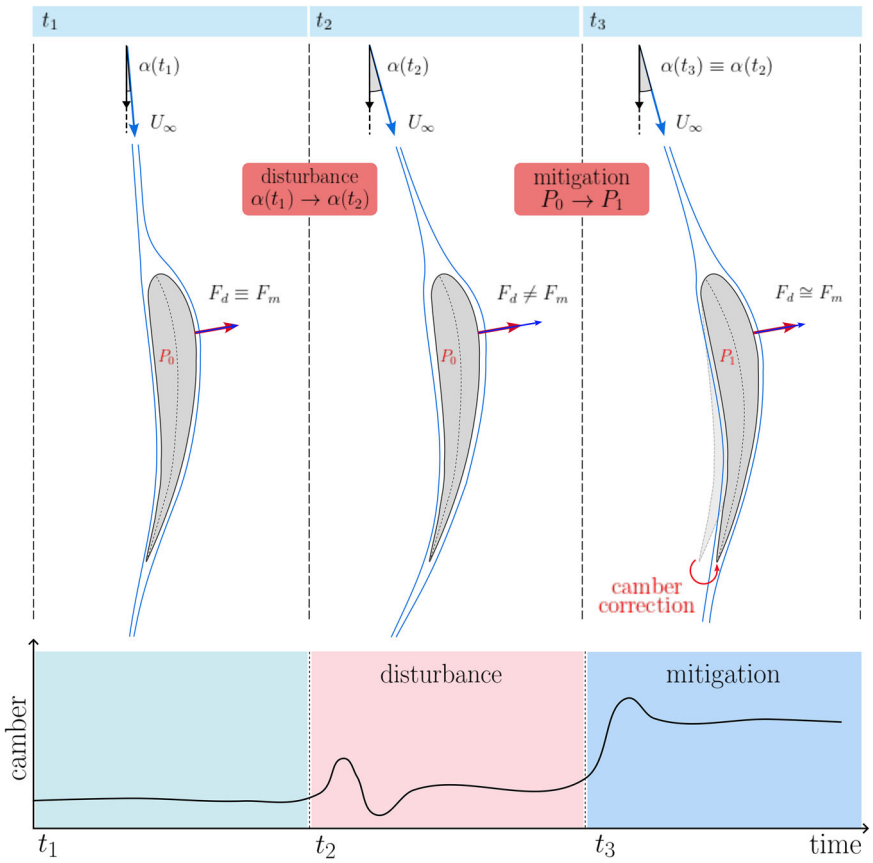

Fig. 4 | Outline of the mitigation process from gust disturbance. Minimisation of unwanted deviation of lift due to gust by means of camber correction. At time t_1, the soft wing is subject to an oncoming flow U_∞ with angle of attack $\alpha(t_1)$ which generates the desired lift force F_m without any actuation P_0 of the camber. At time t_2, following a sudden change of angle of attack from $\alpha(t_1)$ to $\alpha(t_2)$ due to a gust, the new lift F_m experienced by the foil deviates from the desired one, F_d because of a sudden change in camber. By observing this small variation in camber, the foil can autonomously and promptly alter the camber via actuation P_1, reinstating the desired lift even if subject to a perturbed flow direction.

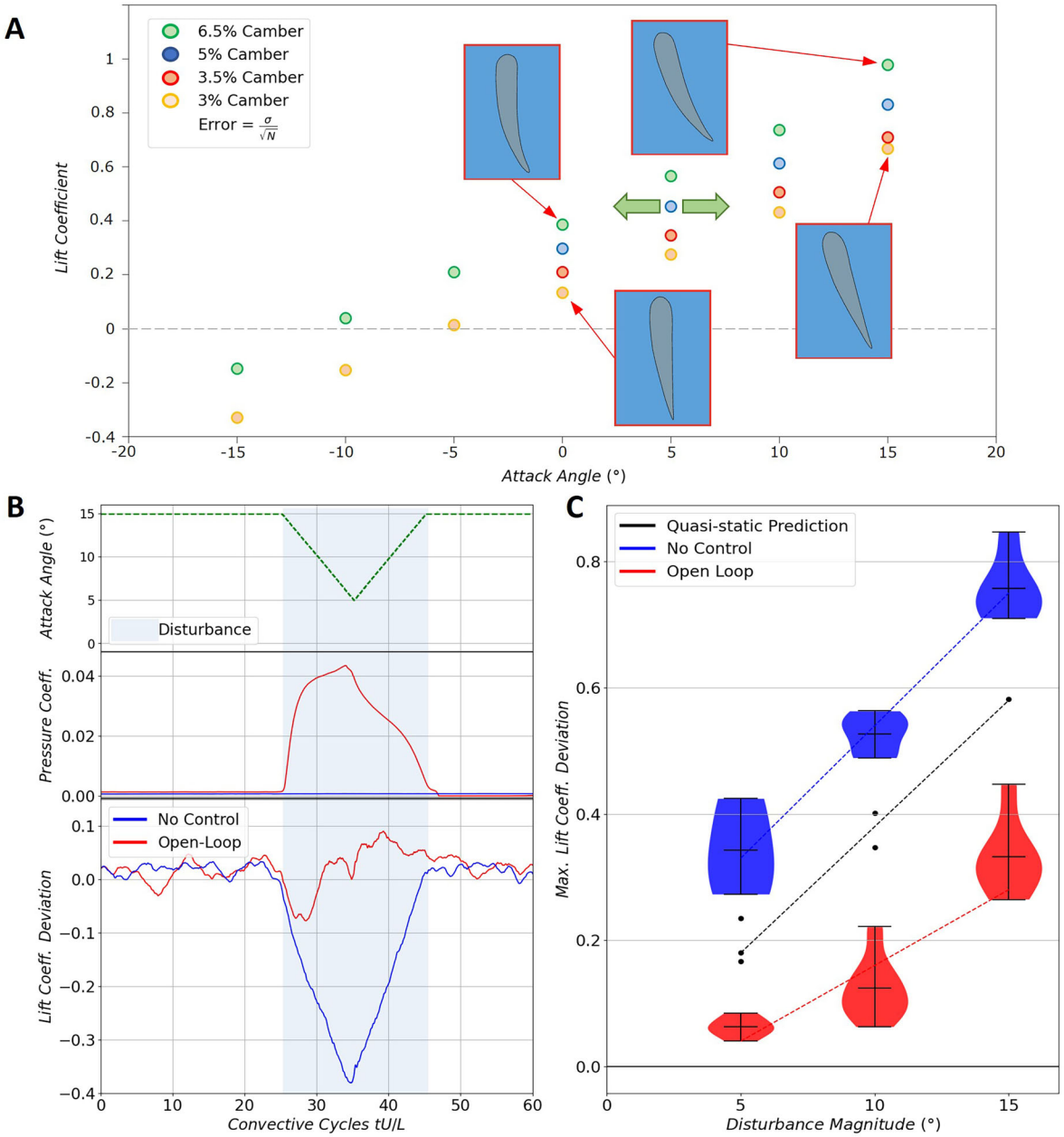

Fig. 5 | Characterisation of morphing wing for disturbance rejection. A Static lift coefficient plotted against angle of attack for 4 cambers. Inserted images show the camber and angle of attack for 2% and 6.5% camber at 0° and 15° angle of attack. The green arrows indicate how a camber change from 6.5% to 2% could allow for lift to be maintained during a 10° angle of attack change disturbance. **B** Open-loop disturbance mitigation: top inset shows the triangle wave disturbance plotted against convective cycles. The disturbance for this experiment is assumed known and a corrective pressure input is scheduled accordingly, as shown in the second inset, where the internal pressure coefficient for the hydraulic actuators is plotted. The bottom inset shows the lift coefficient deviation. Camber variation reduces the effect of disturbances from a 50% decrease in lift coefficient to 10% decrease. **C** Summary of the maximum lift coefficient deviation for triangle wave disturbances of different magnitude where the black markers are the quasi-static disturbance extrapolating between static measurement points in part (**A**).

strategy that leverages assisted-passive response and relies on a minimalist disturbance detection approach. No formal disturbance observer is employed. In the absence of an explicit inversion between lift, camber, and angle of attack, the controller operates as a threshold-based detector on the mean camber deviation and saturates the actuation input to drive the system toward the closest achievable setpoint.

The results from a series of experiments are reported in Fig. 8. Firstly, in Fig. 7, we show an example of the internal pressure, e-skin measured camber, and lift coefficient deviation for the three test cases: non-controlled, open-loop control, and closed-loop control for a square wave gust disturbance. This disturbance is shown in green in Fig. 7A, with an angle of attack change from 15° to 0° in 20 convective cycles. Looking at the non-dimensionalised internal pressure of the hydraulic tubes, Fig. 7B, it is confirmed that the non-controlled case has no change in pressure. The open-loop case is programmed to start pressurising 1.2 s before the onset of the disturbance and to depressurise 1.2 s ahead of the end of the disturbance in order to ensure more effective mitigation of the disturbance.

The closed-loop control follows largely the same temporal profile as the open-loop, but is temporally offset due to the delay necessary for detecting the disturbance. The third section, Fig. 7C, plots the e-skin measured camber for all three cases. The non-controlled case remains mostly constant throughout, with the exception of the beginning and the end of the gust, where the camber undergoes decaying oscillations in response to the gust. This is shown in the *Camber Signature* inset. This signature is what the

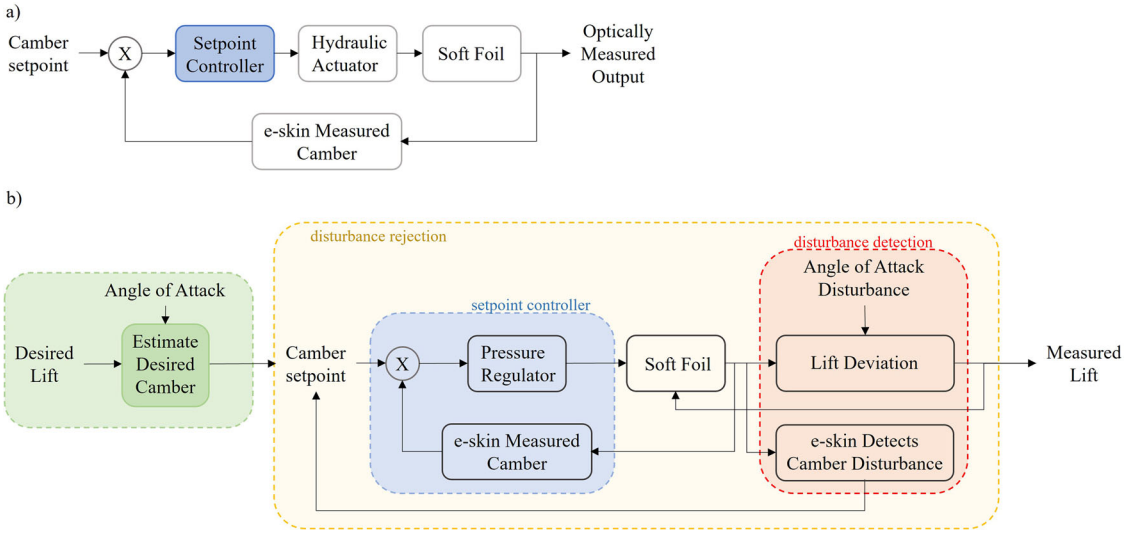

Fig. 6 | Closed loop control for the soft morphing wing. Block diagram outlining the closed loop control structure of the system during (**a**) training and verification of the camber setpoint regulation without angle of attack variation and (**b**) camber setpoint control at arbitrary angles of attack and during disturbance rejection.

closed-loop system is looking to detect to identify the onset of the gust and then respond accordingly.

The signature is visible in the closed-loop control case, following which the camber actuation takes place. The signature is not seen in the open-loop case as the system is already being actuated when the gust begins. Figure 7E shows images of the camber at different stages of the experiment. Before and after the gust, all cases are identical. During the gust, the non-controlled case (blue) maintains a constant camber, which causes it to experience a large negative change in lift. Both open-loop (red) and closed-loop (purple) cases, actively increase the camber to mitigate the disturbance. The system was successful in detecting 70% of square wave gusts, but was found unable to detect triangle wave gusts as the change in force was too gradual.

The section of Fig. 7D plots the lift coefficient deviation for the three cases. The non-controlled case exhibits a large drop in lift coefficient compared to either open-loop or closed-loop controlled cases. Both controlled cases, after an initial disturbance, settle to a value of almost zero lift deviation, with the closed-loop controlled case reaching this value more slowly owing to the delay required to detect the gust. Similarly, we see a large effect at the end of the gust returning to the initial conditions from the closed-loop case, again due to the delay required to detect the disturbance.

Figure 8 plots the impulse per unit area of the wing against convective cycles for the three test cases, along with the analytical solution for an idealised rigid wing NACA3515 profile. Such wing profile was chosen as the most similar to the geometry of the wing section used in these experiments. Impulse, Fig. 8A, B, is a useful integral metric to better visualise the amount of energy transferred from the gust to the foil during the disturbance: the lower the impulse, the more succesful the disturbance rejection task is. This representation interestingly shows that even the non-controlled case outperforms the rigid wing by three fold owing to its flexible nature. This is not a surprise when we consider the passive drag reduction seen in plants and leaves[58]. Both controlled cases outperform the non-controlled case by a similar margin.

Figure 8B summarises the maximum absolute impulse experienced by the wing for positive and negative gusts as schematically depicted in Fig. 8C. The controlled cases are able to significantly reduce the gust effect for positive and negative gusts. Crucially, the closed-loop case is only marginally outperformed by the open-loop case and is able to detect and mitigate gusts in both directions.

Discussion

We have demonstrated a rapidly morphing proprioceptive soft wing for underwater vehicle disturbance rejection with a response time up to four times faster than comparable morphing wings with increased range[29,31], and five orders of magnitude less energy than applications that harness thermal energy to change morphology[59].

Disturbance rejection using shape morphing is achievable because the same lift coefficient is attainable at different angles of attack by adjusting the camber, as indicated in Fig. 5A and because the soft nature of the wing spontaneously mitigates part of the disturbance. A disturbance in the form of an angle of attack change could therefore be mitigated by changing the camber at the right time and rate. The outcome of this mitigation method is shown in the bottom section of Fig. 5B where the lift coefficient deviation is plotted. The ideal case would have zero lift deviation and completely mitigate a triangle wave disturbance. The prescient open-loop control case almost achieves this, reducing the impact from a 50% decrease in the lift coefficient to a 10% decrease. This shows that camber morphing is an effective method for disturbance mitigation when combined with passive properties of the soft wing. Controlling the camber has obvious benefits for disturbance mitigation over non-controlled cases. The residual disturbance effect could be further mitigated in the open-loop controlled cases with faster hydraulic actuators and an observer.

Moreover, we showcase the ability of fine control shape estimation, using a built-in capacitive e-skin, to detect a 20 convective cycle square wave disturbance input, Fig. 7. The system was successful in detecting 70% of square wave gusts (both positive and negative) and can be improved with a dedicated disturbance observer[60]. The current limitation in the system for faster response times is the linear actuator that adjusts the internal pressure. This could be improved with a more powerful actuator. The sensing and control system is capable of responding at 30 Hz in the current configuration. In addition, this method of underwater shape estimation is well suited for progression to more complex systems as it is agnostic to the shape of the underlying body, making it suitable for more complex morphologies or modes of deformation, such as fish bodies, and multidimensional disturbances.

When tested for various degrees of disturbances, the closed-loop controller was found to reduce the maximum impulse of a comparable rigid wing by 87%, Fig. 8. In the absence of documented disturbance-rejection performances for underwater specimens, this result places the wing's capability at roughly double the gust-impulse mitigation of an owl's rejection manoeuvre[28], with due caution in interpreting this cross-domain comparison. The non-controlled flexible wing outperforms the rigid wing by threefold in this metric and both controlled cases outperform the non-controlled, purely passive case by a similar margin. The controlled cases do significantly better than non-controlled and rigid cases at large disturbances,

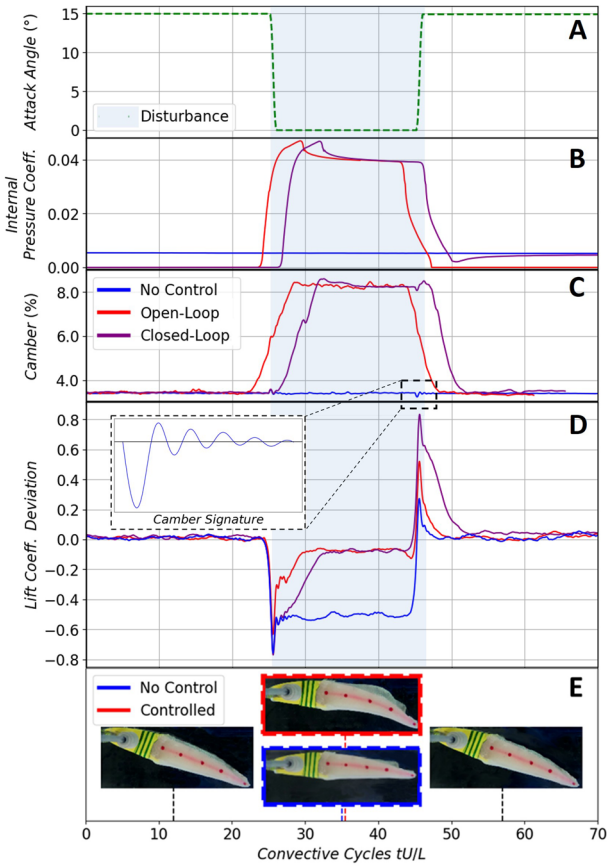

Fig. 7 | Example of a closed-loop disturbance rejection experiment. A disturbance in terms of angle of attack of the wing plotted against convective cycles: this corresponds to a 20 s gust square wave disturbance. **B** the non-dimensionalised internal pressure coefficient for the internal stiffening tubes, indicating the onset of actuation. **C** the e-skin measured camber for each of the test cases with the inset showing the camber signature that the controller is trying to detect. **D** the lift coefficient deviation for three different test cases (the ideal case would suffer no lift deviation). The open-loop controlled case is scheduled and starts mitigation immediately before disturbance takes place. The closed-loop controlled case is delayed relative to the open-loop as it necessitates disturbance to be detected first. **E** the geometry of the wing before and after the disturbance, as well as the difference between the controlled and non-controlled cases during the disturbance shown in red and blue respectively.

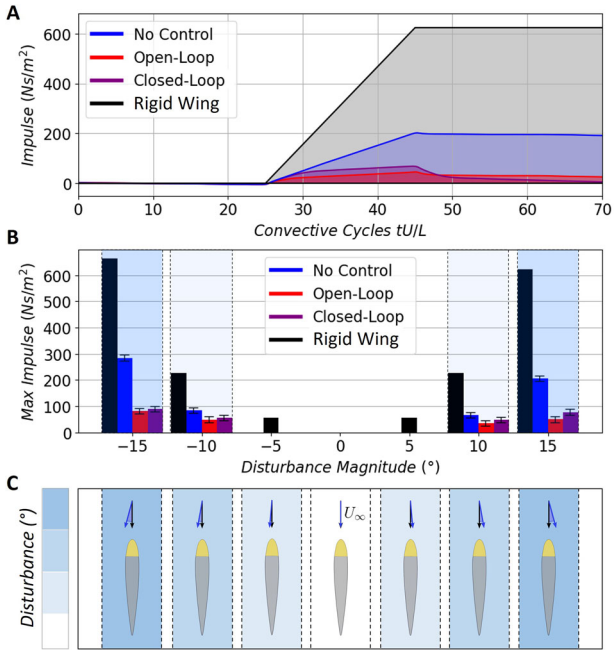

Fig. 8 | Summary of closed-loop disturbance rejection experiments. A The impulse per unit area of wing is plotted against convective cycles for the three test cases and the analytical solution for an idealised rigid wing with a NACA3515 profile shape. The flexible foil outperforms the rigid foil even without control. Both controlled cases have further reduced impulse. **B** The absolute value of the maximum impulse experienced by each test case is plotted for each magnitude of disturbance along with the rigid NACA3515 profile. The controlled cases do significantly better than non-controlled and rigid cases at large disturbances but at smaller disturbances they depend on actuation response time. **C** Deviation of AoA per each case shown.

but have a benefit limit at smaller disturbances due to the response time of the hydraulic actuator.

Comparing the total impulse on the system integrated over the whole disturbance event, both open-loop and closed-loop controlled cases settle to a value of almost zero lift deviation, with the open-loop controlled case reaching this value more slowly owing to the delay required to detect the gust. The closed-loop case exhibits a higher maximum impulse, but the delayed response results in a final impulse that is closest to zero $N\,s\,m^{-2}$.

These findings illustrate how the intrinsic softness of the body can contribute to disturbance rejection through a balance of passive compliance and active control. When coupled with proprioceptive sensing, this hybrid strategy enables more robust responses to environmental perturbations, echoing the mechanisms observed in flying and swimming organisms that must maintain manoeuvrability under rapidly changing conditions. While the present results demonstrate good performance in a controlled setting with a single wing section, translating this approach to fully autonomous vehicles will demand significant advances in scalability, integration, and control architectures. For example, to implement this system on an AUV (such as in Fig. 1) the sensor array would need to integrate between soft and rigid components in a way that is more robust to wear and tear, which is a common challenge for soft robotic implementation in general. Additionally, there are manufacturing and training challenges for increasing scale as you would expect for an AUV. Nevertheless, such techniques may ultimately help bring engineered systems closer to the performance of living organisms, even in challenging environments.

Methods

Morphing Soft Wing

We designed, built and tested a tunable-stiffness wing section using our previously developed second-moment-of-area hydraulic actuation (Fig. 2C)[57]. The wing section is comprised of a rigid nose connected to a soft tail. Embedded within the tail are two inflatable elastic tubes. The tail has a base stiffness provided by the silicone, and the tubes can be pressurised to increase the second-moment-of-area and stiffness. The actuators provide authority over the stiffness and camber with increasing pressure, which results in the deformation of the foil in the form of increasing camber[57]. The system is actuated hydraulically to avoid compressibility effects and negate buoyancy forces (Fig. 2). Additional specifications are provided in Table 1.

Hydraulic actuation affects the planar curvature of the wing section, which is expressed here by the camber. The camber of a wing is described by its maximum value along the foil length as depicted in Fig. 3C and expressed according to

$$camber\,\% = 100 \times \frac{(Ch_n, C_n)_{max}}{Ch} \quad (1)$$

where Ch is the chord length, and $(Ch_n, C_n)_{max}$ is the maximum perpendicular distance between the chord line and the camber line, hence camber is given as a percentage. For a prescribed angle-of-attack α, a change in camber of a wing results in changes in lift and drag forces. Typically, wing cambers are in the range of 0-10%. For these experiments, a camber range of 2.5–8.5% is used. These values are selected to be within the range of typical

Table 1 | Experimental Materials

Stiffness foil		
Part	*Material*	*Dimensions (mm)*
Soft Tail	EcoFlex-30	120 x 140 x 30
Rigid Nose	Polylactic Acid Plastic	120 x 80 x 30
Inflatable Tubes	Isobutylene Isoprene Rubber	110 x 15 x 15
Square Bar	Aluminium	700 x 10 x 10
e-skin	EcoFlex-30, EGaIn	120 x 140 x2
Training Set Up		
DAQ	Bespoke Measurement Board	
Motor Driver	Cytron MD10C	
Controller	Arduino Uno	
Camera	GoPro HERO 10	
Resolution	1920 x 1080	
Frame Rate	30 fps	

wing cambers for hydrodynamic performance, offering a range of possible lift coefficients.

Underwater E-skin

We developed a liquid metal-based e-skin for proprioceptive sensing of the flexible foil, Fig. 2A. Figure 9 shows the fabrication process and design of the capacitive e-skin. This consists of a silicone layer, six copper and EGaIn liquid metal (75.5% eutectic gallium, 24.5% indium) electrodes and a sealing layer. The overall dimensions are $120 \times 112 \times 2\ mm^3$. The contact area of each electrode with the conductive layer is $5 \times 5\ mm^2$. The asymmetric 'L' shaped channels are designed to best capture both chordwise and spanwise curvature. A silicone elastomer, made of Ecoflex 00-30 (Smooth-On Inc.), is cast in a 3D printed mould to create vacant channels for the liquid metal. The cured silicone is removed from the mould and bonded with a new silicone layer using uncured silicone mixture as the adhesive. No release agent is used. Liquid metal is injected using a syringe into the hollow channels with a second needle used as an exhaust for the air. The holes created by the needles are then sealed with additional silicone.

The sensor operates by measuring the relative capacitance of select pairs of close proximity liquid metal electrodes. Intuitively, due to signal attenuation, the strongest signals come from adjacent pairs. This is also evident experimentally. As a result, we selected nine specific pairs of electrodes: (1, 2), (1, 3), (2, 3), (2, 4), (3, 4), (3, 5), (4, 5), (4, 6), and (5, 6), Fig. 9f. When the shape of the e-skin changes due to deformation of the underlying foil, the relative capacitance between electrode pairs varies accordingly. By normalising the sensor readings against the undeformed shape readings, it is possible to use the capacitance signal to sense the foil's change in shape. Each readout is normalised as follows

$$c = \frac{(c' - c_o)}{c_o} \tag{2}$$

where c is the normalised capacitance readout, c' is the absolute readout, and c_o is the reference untrained readout. The sensor operates by measuring the relative capacitance of select pairs of proximity liquid metal electrodes with the strongest signals coming from adjacent pairs. To quantify this change in shape, a model must be trained based on images of the robot taken at matching timestamps to the sensor readings, Fig. 2B, D. Upon successful training, reliance on the external visual feedback is no longer required.

Figure 2C shows the capacitive e-skin connected to the wing section and Fig. 2B the raw sensor reading at various stages of the wing curvature, Fig. 2D.

Training the e-skin for underwater camber estimation is performed in a static water tank, as shown in Fig. 10. Training the e-skin for hybrid passive-active disturbance detection and rejection is performed in flow, as shown in Fig. 3.

Underwater E-skin Training

Figure 10 shows the experimental setup for training and testing of the e-skin on the soft robotic foil. For the collection of training data, the foil is actuated for ten cycles with 30 s of baseline data taken before and after actuation. The pressurisation of the foil is controlled using a linear actuator connected to a syringe which supplies the pressure. An underwater camera records the motion of the foil for training and ground truth comparison. The e-skin samples at 714 Hz and the camera at 30 Hz. The video is post-processed to track the five red markers and convert these to sets of five two-dimensional coordinates for each image. The coordinate sets and time-corresponding training data are then employed to train a Multilayer Perceptron (MLP) model which ultimately allows association of instantaneous capacitance readouts to foil shape, thus removing the need for visual feedback.

An MLP model is used due to its suitability at handling structured data like the sensor readings from the e-skin, and it is able to capture complex non-linear relationships between the input sensor data and the output coordinates which would be expected from a more complex three-dimensional problem. Compared to recurrent or convolutional neural networks, the MLP is an effective, and more simplistic, choice for accurately estimating the foil shape from the sensor data as well as facilitating future expansion to 3D deformations. The MLP model (Table 2) has one input layer, three hidden layers, and one output layer. The input of this model is the nine calibrated capacitance readouts in one frame from the e-skin. The output is a vector with a size of 10, indicating the coordinates of the five markers which can be used to calculate the camber.

During training, the foil's leading edge is kept stationary, allowing for the camber line of the foil to be accurately described by 6 geometrical points. A spline is fitted to populate the points from the trailing edge to the start of the silicone and the chord line is calculated from the leading edge to the trailing edge; eqn. (1) provides instantaneous estimate of the foil camber based on these two lines. Accuracy of the e-skin, in still water, in estimating camber is reported in supplementary video S1.This training process is repeated in flow for the hybrid passive-active disturbance detection and rejection.

In Summary:

- The e-skin reads in nine capacitance signals at a given time, *t*.
- The video post-processing produces five sets of marker coordinates in space, relative to the fixed leading edge point, for the same time, *t*.
- The MLP model takes all sets of capacitance signals and marker coordinates for all training data times to train the model.
- Once trained, the model predicts the 5 point locations based on new capacitance signals, accounting for noise within the signals.
- A spline is fitted to the 5 predicted points and the maximum camber calculated.
- The camber is used as the single control variable from the 9 input signals.

Underwater Testing

Camber setpoint regulation relies on instantaneous e-skin readouts and the control loop presented in Fig. 6A; results demonstrate the capability to perform accurate dynamic trajectory tracking on the wing's camber, as demonstrated in Figs. 11, 12 and in the supplementary video S2.

The underwater disturbance rejection experiments took place in the University of Southampton recirculating water tunnel: Fig. 3A shows the experimental set up within the flume. The wing section is placed so that its lower edge is 1.5 chord lengths from the bottom of the channel. Surface plates are placed the same distance above the upper edge to remove free surface effects. The stepper motor, gearbox, and encoder mount are fixed directly to the flume. The shaft from the stepper motor runs through the optical encoder and is connected to a 3D-printed adaptor, which holds the load cell in place. The shaft of the wing is connected to the load cell with a second 3D-printed adaptor. The underwater camera is used for training the

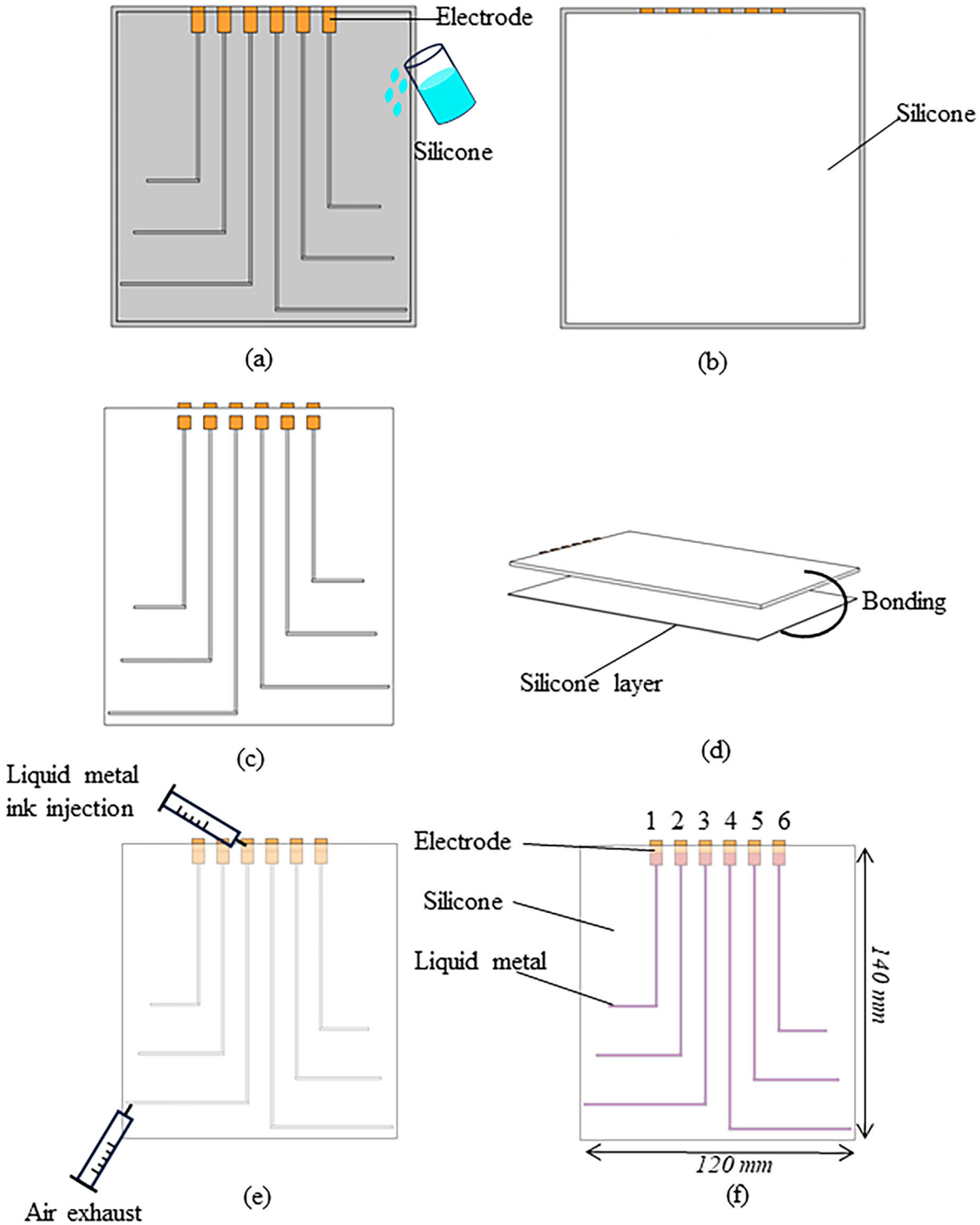

Fig. 9 | Fabrication process of the capacitive e-skin. a Deployment of copper electrodes on the 3D-printed mould, **b** Eco-flex 00-30 is poured into the 3D printed mould, **c** curing of the top layer at room temperature for 4 h and release the mould, **d** fabrication of an additional silicone backing layer and bonding with the top layer by means of the uncured silicone mixture as the adhesive, **e** injection of Liquid metal into the hollow channels with a second needle used as an exhaust for the air and finally sealing of the holes created by the needles with additional silicone. **f** The fabricated Liquid metal e-skin.

e-skin only. The load cell rotates with the wing so the encoder is necessary for both measuring the angle of the wing but also translating the forces from the local coordinate system to the stream-wise coordinate system (Fig. 3C).

The flow velocity is 0.2 $m\,s^{-1}$, which is equivalent to one chord length per second. For initial characterisation, static lift measurements are carried out. Forces are recorded for 200 convection cycles at 1000 Hz. at four cambers from -15° to 15° in increments of 5°. The concept of camber change as a means of mitigating gusts is verified by comparing lift deviation response for a scheduled open-loop pressure change to a non-controlled case for a variety of magnitudes and directions (± 5°, 10°, 15°), and durations (5 s, 10 s, 20 s. 30 s) of triangle wave gusts.

Detection of the disturbance involves the camber dynamic response being compared against a characteristic gust-induced excitation and deemed as such if comprised within a pre-determined confidence tolerance.

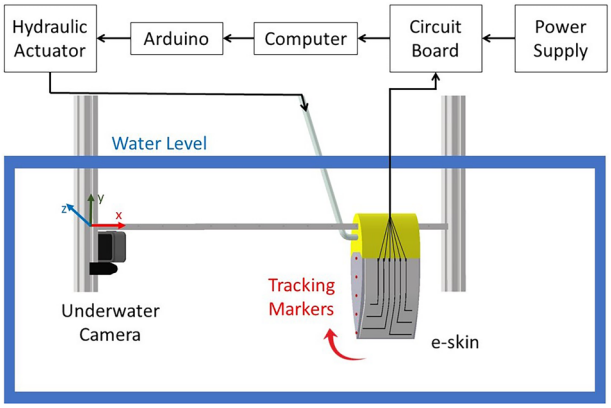

Fig. 10 | Schematic of the static testing set up. The pressurisation of the foil is controlled using a linear actuator connected to a syringe which supplies the pressure. An underwater camera records the motion of the foil for training and ground truth comparison.

Table 2 | TRAINING SPECIFICATIONs

MLP	
Neurons per hidden layer	32, 128, 32
Training Method	Mean Squared Error (MSE)
	loss function
Learning Rate	0.0001
Batch size	256
Training Data	24,000 frames
Training, Validating, Testing Ratio	70/20/10
Minimum validation loss	0.397
PID Controller Gains	
K_p, K_i, K_d	50, 1, 1

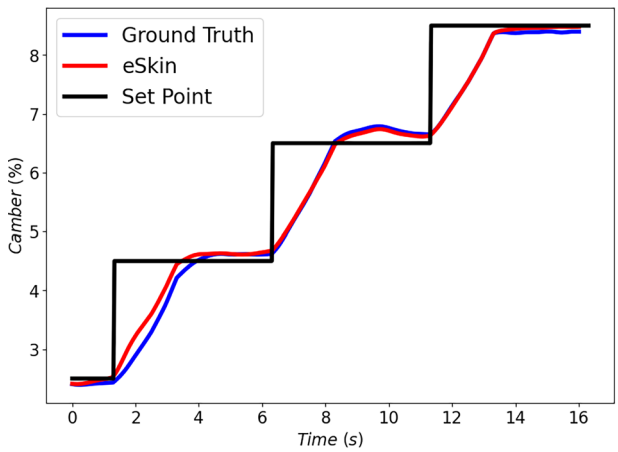

Fig. 11 | Plot of camber against time for a 2% camber step increase every 5 seconds from 2.5% to 8.5% (equivalent to a tip amplitude change of 10 mm per step) with a rise time of 1.7 s. Plotted is the instantaneous foil camber based on the e-skin and the ground truth measurement from the camera point-tracking, averaged across 10 trials.

Upon detection of the oscillation, the controller identifies the direction change of the oncoming gust based on the perceived change in the camber and commands the actuator accordingly to mitigate the effect of the gust on the lift coefficient. A schematic of this control loop is shown in Fig. 6b and an example of a disturbance rejection test is demonstrated in supplementary video S3.

For real-world applications, the system needs to be able to reach a desired set point with different time scales and paths. For this work, we tested a step function with 2% camber increases every 5 s, and triangle and sinusoidal motion profiles. The motion profiles were tested at 20, 10, and 5 s periods around a mean value of 4.25% and amplitudes of 5 and 2%. Faster response times were not achievable due to the speed limitations of the linear actuator used to control the pressure.

The control loop is depicted in Fig. 6a. Relative capacitance measurements are read and the MLP model converts the signals into coordinates from which the camber is calculated. A PID controller compares the measured position to the set point and drives an input to the hydraulic actuator. Parameters for the MLP and PID were determined through preliminary experiments, and are given in Table 2.

Underwater wing camber setpoint regulation

Figure 11 shows camber time history for a 2% camber step increase every 5 s from 2.5% to 8.5%. This is equivalent of a wing tip position change of 10 mm per step. Plotted is the estimated position of the robot based on the e-skin measurement and the ground truth position of the robot based on the camera point-tracking, averaged across 10 trials. The rise time is 1.7 s.

Figure 12a shows the mean phase averaged camber plotted for six set point motion profiles. The top row corresponds to sine wave inputs. The bottom row corresponds to Triangle wave inputs. Each profile has a peak-to-peak amplitude of 2% and a mean of 4.25% and each column corresponds to a period of 20, 10, 5 s from left to right, respectively. Plotted is the estimated position of the robot based on the e-skin measurement and the ground truth position of the robot based on the camera point-tracking, averaged across 20 cycles. These results show excellent set point regulation for the 10 s period and even for the faster 5 s actuation routine.

Figure 12b shows mean phase averaged camber plotted for the same six set point motion profiles, with a new peak-to-peak amplitude of 5%, averaged across 20 cycles. The positional error observed for the 5 s period is mainly due to the slow response of the hydraulic actuator, as expected given the rise time measured in Fig. 11. We see increased errors between the sensor and the ground truth for the 5 s period also. This is likely being caused by the dynamics of the system causing hydrodynamic pressure from added mass that was not present in the training data. Discrepancies for the 20 and 10 s cases for both the 2% and 5% tests are attributed to high frequency signal noise.

Figure 13 reports on the e-skin state estimation performance in still water by comparing the measurement error between the e-skin and the ground truth as a percentage of the foil length at different camber magnitudes. The foil is calibrated (eqn. (2)) based on the 2% camber zero position so there is higher accuracy at this point. Plotted is the mean error, the first standard deviation, σ, of the error and the maximum and minimum error values measured for all data. We demonstrate a maximum sensor error of less than 2.2% and an average sensor error of 0.52%. These errors are extremely small and acceptable given hydrodynamic considerations in unsteady natural flow. We see a peak in error around 3% camber, because at relatively low camber values there is smaller overall deformation of the foil which leads to a worse signal-to-noise ratio and induces higher average error.

Figure 14 assesses the closed-loop control performance by comparing the error between set point and ground truth measurement for triangle and sinusoidal wave inputs at 2% and 5% camber variation. Plotted is the Root Mean Square Error normalised by the average signal magnitude: $RMSE/\bar{y}$ (NRMSE). NRMSE decreases with a longer period due to the speed of actuation capabilities. NRMSE also decreases with a smaller desired amplitude due to the slower operation required and more linear response of the system. There is little difference in error between the triangle and sinusoidal wave setpoints.

The results presented give confidence in the robustness and accuracy of the underwater e-skin for the purpose of control of the flexible wing and in their implementation for the disturbance rejection tasks.

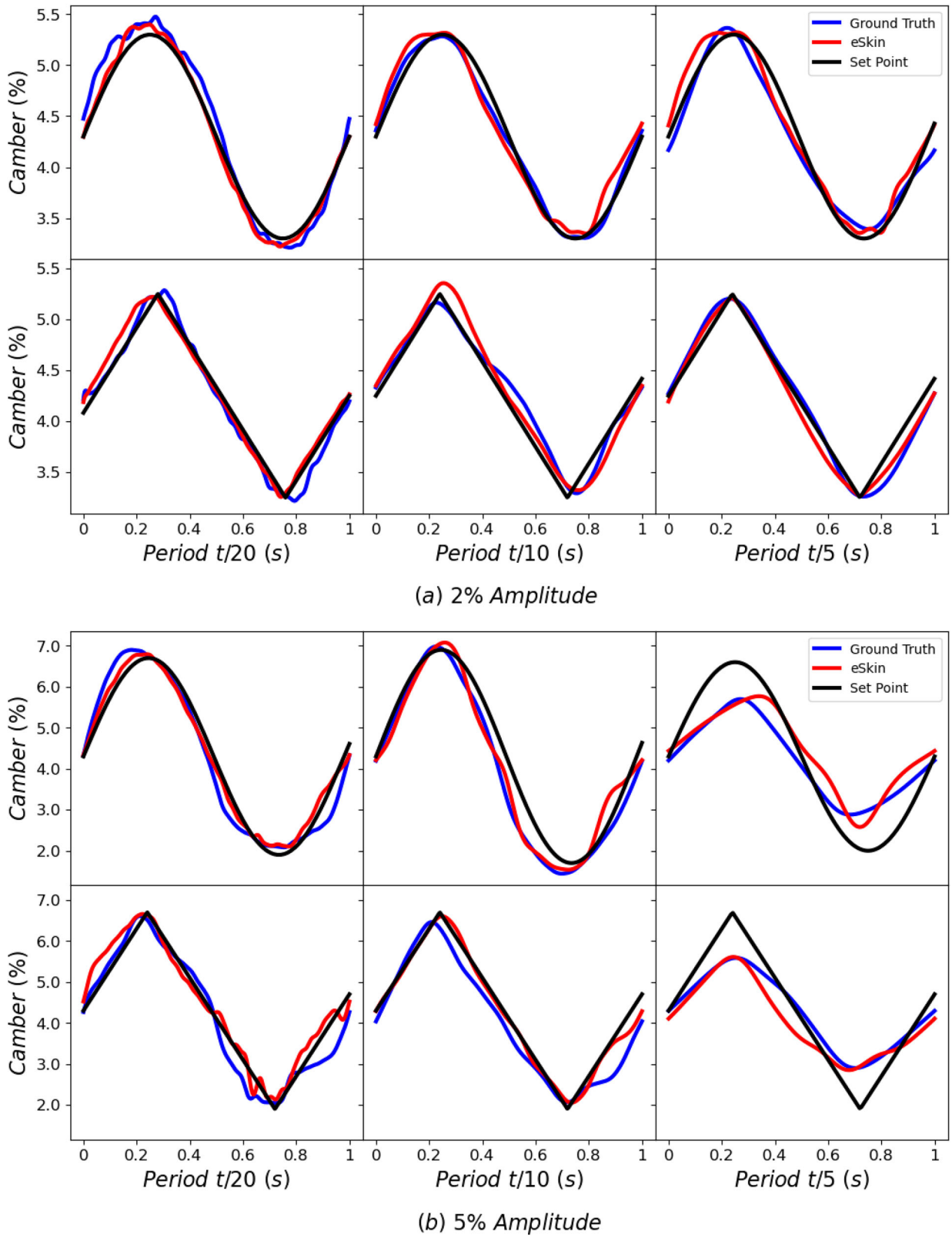

Fig. 12 | Camber set point regulation. a Mean phase averaged camber plotted for six set point motion profiles. The top row correspond to sine wave inputs. The bottom row corresponds to Triangle wave inputs. Each profile has a peak-to-peak amplitude of 2% and a mean of 4.25%. Each column corresponds to a period of 20 s, 10 s, 5 s from left to right respectively. Plotted is the estimated position of the robot based on the e-skin measurement and the ground truth position of the robot based on the camera point-tracking, averaged across 20 cycles. **b** The same motion profiles are plotted, changing the peak-to-peak amplitude to 5%.

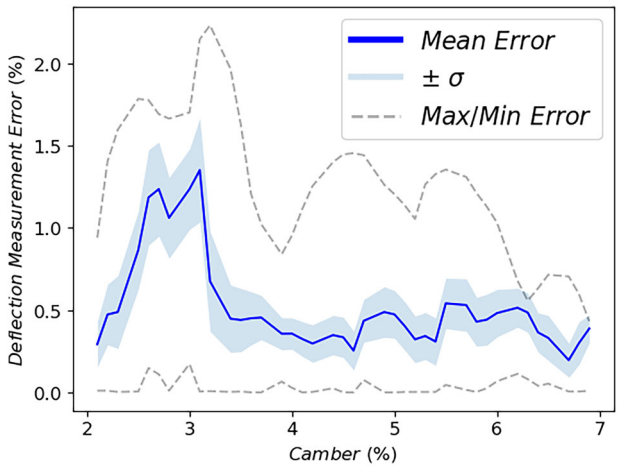

Fig. 13 | Comparison of the measurement error between the e-skin and the ground truth as a percentage of the foil length at different camber magnitudes. Plotted is the mean error, the first standard deviation, σ, of the error and the maximum and minimum error values measured.

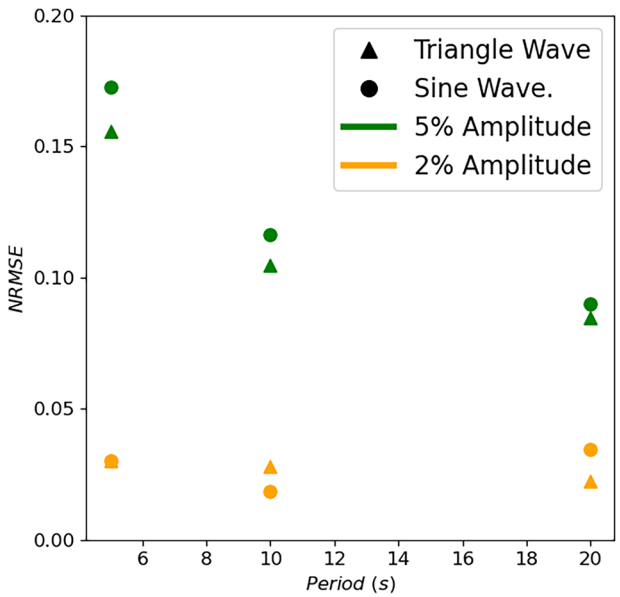

Fig. 14 | Comparing the error between set point and ground truth measurement for triangle and sinusoidal wave inputs at 2% and 5% camber variation. Plotted is the Root Mean Square Error normalised by the average signal magnitude: $RMSE/\overline{y}$ (NRMSE).

Data availability

Supplementary data S1 is provided reporting a sample of the experimental results employed for the closed-loop disturbance rejection tests presented in the Results section, Fig. 7. The entire experimental dataset is available at https://doi.org/10.5258/SOTON/D3190.

Received: 27 September 2025; Accepted: 28 January 2026;
Published online: 12 February 2026

References

1. Harvey, C. & Inman, D. J. Gull dynamic pitch stability is controlled by wing morphing. *Proc. Natl. Acad. Sci. USA* **119**, e2204847119 (2022).
2. Majumdar, D., Ravi, S. & Sarkar, S. Passive dynamics regulates aperiodic transitions in flapping wing systems. *PNAS Nexus* **2**, pgad086 (2023).
3. de Langre, E. Effects of wind on plants. *Annu. Rev. Fluid Mech.* **40**, 141–168 (2008).
4. Brown, R. E. & Fedde, M. R. Airflow sensors in the avian wing. *J. Exp. Biol.* **179**, 13–30 (1993).
5. Horster, W. Histological and electrophysiological investigations on the vibration-sensitive receptors (herbst corpuscles) in the wing of the pigeon (Columba livia). *J. Comp. Physiol. A* **166**, 663–673 (1990).
6. Martinez Groves-Raines, M. et al. Steady as they hover: kinematics of kestrel wing and tail morphing during hovering flights. *J. Exp. Biol.* **227**, jeb247305 (2024).
7. Cheney, J. A. et al. Bird wings act as a suspension system that rejects gusts: bird wings act as a suspension system. *Proc. R. Soc. B Biol. Sci.* **287**, 20201748 (2020).
8. BLECKMANN, H. & ZELICK, R. Lateral line system of fish. *Integr. Zool.* **4**, 13–25 (2009).
9. Iv, R. W., Neubarth, N. & Hale, M. E. The function of fin rays as proprioceptive sensors in fish. *Nat. Commun.* **4**, 2751 (2013).
10. Bleckmann, H. et al. *Station Holding of Trout: Behavior, Physiology and Hydrodynamics*, 161–177 https://doi.org/10.1007/978-3-642-28302-4_10 (Springer, 2012).
11. Gibbs, B. J., Akanyeti, O. & Liao, J. C. Kinematics and muscle activity of pectoral fins in rainbow trout (oncorhynchus mykiss) station holding in turbulent flow. *J. Exp. Biol.* **227**, jeb246275 (2024).
12. Drucker, E. G., Walker, J. A. & Westneat, M. W. Mechanics of pectoral fin swimming in fishes. In *Fish Biomechanics*, vol. 23 of *Fish Physiology*, 369–423 https://www.sciencedirect.com/science/article/pii/S1546509805230108 (Academic Press, 2005).
13. Quinn, D. & Lauder, G. Tunable stiffness in fish robotics: mechanisms and advantages. *Bioinsp. Biomimetics* **17**, 011002 (2022).
14. Aiello, B. R., Westneat, M. W. & Hale, M. E. Mechanosensation is evolutionarily tuned to locomotor mechanics. *Proc. Natl. Acad. Sci.* **114**, 4459–4464 (2017).
15. Ji, H., Fouad, A. D., Li, Z., Ruba, A. & Fang-Yen, C. A proprioceptive feedback circuit drives caenorhabditis elegans locomotor adaptation through dopamine signaling. *Proc. Natl. Acad. Sci. USA* **120**, e2219341120 (2023).
16. Gazzola, M., Argentina, M. & Mahadevan, L. Gait and speed selection in slender inertial swimmers. *Proc. Natl. Acad. Sci. USA* **112**, 3874–3879 (2015).
17. Walker, J. A. Kinematics and performance of maneuvering control surfaces in teleost fishes. *IEEE J. Ocean. Eng.* **29**, 572–584 (2004).
18. Pebody, M. Autonomous underwater vehicle collision avoidance for under-ice exploration. *Proc. Inst. Mech. Eng. Part M: J. Eng. Marit. Environ.* **222**, 53–66 (2008).
19. Gemmell, B. J. et al. Passive energy recapture in jellyfish contributes to propulsive advantage over other metazoans. *Proc. Natl. Acad. Sci. USA* **110**, 17904–17909 (2013).
20. Nishida, Y. et al. Hovering type auv "tuna-sand" and its surveys on smith caldera in izu-ogasawara ocean area. In *2013 OCEANS - San Diego*, 1–5 (OCEANS, 2013).
21. Facility, N. D. S. Sentry one page https://www.whoi.edu/wp-content/uploads/2019/02/18G0622-Sentry-One-Pager-Masako-Mtominaga.pdf (WHOI, 2019).
22. Hydroid A Kongsberg, c. Remus 600 autonomous underwater vehicle https://www.kongsberg.com/globalassets/maritime/km-products/product-documents/remus-600 (KONGSBERG, 2019).
23. Fisher, C. R. et al. Footprint of deepwater horizon blowout impact to deep-water coral communities. *Proc. Natl. Acad. Sci. USA* **111**, 11744–11749 (2014).
24. Walker, K. L., Jordan, L.-B. & Giorgio-Serchi, F. Nonlinear model predictive dynamic positioning of a remotely operated vehicle with wave disturbance preview. *Int. J. Robot. Res.* https://doi.org/10.1177/02783649241286909 (2024).
25. Dantas, J. & de Barros, E. Numerical analysis of control surface effects on AUV manoeuvrability. *Appl. Ocean Res.* **42**, 168–181 (2013).
26. Bowker, J. & Townsend, N. Evaluation of bow foils on ship delivered power in waves using model tests. *Appl. Ocean Res.* **123**, 103148 (2022).

27. Wang, X., Mkhoyan, T., Mkhoyan, I. & De Breuker, R. Seamless active morphing wing simultaneous gust and maneuver load alleviation. *arXiv* 1–26 2012.14520 (2020).
28. Chowdhury, J. & Ringuette, M. J. Effect of a rotating and swept wingtip on streamwise gust alleviation. *AIAA J.* **59**, 800–811 (2021).
29. GU, X. et al. Integrated optimization design of smart morphing wing for accurate shape control. *Chin. J. Aeronautics* **34**, 135–147 (2021).
30. Yang, G., Guo, H. & Liu, R. Design and analysis of a variable-span and cambered span morphing wing for UAV. *IEEE International Conference on Robotics and Biomimetics, ROBIO 2019* 1318–1324 (IEEE, 2019).
31. Wang, Z., Yang, X. & Li, B. SMA-actuated morphing wing with varying spanwise curvature and sweptangle. *IEEE International Conference on Robotics and Biomimetics, ROBIO 2019* 1615–1620 (IEEE, 2019).
32. Li, B. et al. A flexible morphing wing by soft wing skin actuation utilizing dielectric elastomer: experiments and electro-aerodynamic model. *Smart Mater. Struct.* **29**, 0150321 (2020).
33. Baines, R. et al. Multi-environment robotic transitions through adaptive morphogenesis. *Nature* **610**, 283–289 (2022).
34. Wang, X. et al. Bioinspired intelligent soft robotics: from multidisciplinary integration to next-generation intelligence. *Adv. Sci.* **n/a**, e06296 (2025).
35. Fang, J. et al. A shift from efficiency to adaptability: recent progress in biomimetic interactive soft robotics in wet environments. *Adv. Sci.* **9**, 2104347 (2022).
36. Alben, S., Witt, C., Baker, T. V., Anderson, E. & Lauder, G. V. Dynamics of freely swimming flexible foils. *Phys. Fluids* **24**, 051901 (2012).
37. Shelton, R. M., Thornycroft, P. J. M. & Lauder, G. V. Undulatory locomotion of flexible foils as biomimetic models for understanding fish propulsion. *J. Exp. Biol.* **217**, 2110–2120 (2014).
38. Giordano, A. et al. A soft robotic morphing wing for unmanned underwater vehicles. *Adv. Intell. Syst.* **6**, 2300702 (2024).
39. Zhong, Q. et al. Tunable stiffness enables fast and efficient swimming in fish-like robots. *Sci. Robot.* **6**, 4088 (2021).
40. Fish, F. & Lauder, G. Passive and active flow control by swimming fishes and mammals. *Annu. Rev. Fluid Mech.* **38**, 193–224 (2006).
41. Wang, H., Totaro, M. & Beccai, L. Toward perceptive soft robots: progress and challenges. *Adv. Sci.* **5**, 1800541 (2018).
42. Youssef, S. M. et al. Underwater soft robotics: a review of bioinspiration in design, actuation, modeling, and control. *Micromachines* **13**, 1–16 (2022).
43. Hegde, C. et al. Sensing in soft robotics. *ACS Nano* **17**, 15277–15307 (2023).
44. Peng, R., Wang, Y. & Lu, P. A tendon-driven continuum manipulator with robust shape estimation by multiple IMUs. *IEEE Robot. Autom. Lett.* **9**, 3084–3091 (2024).
45. Park, Y.-L., Chen, B.-R. & Wood, R. J. Design and fabrication of soft artificial skin using embedded microchannels and liquid conductors. *IEEE Sens. J.* **12**, 2711–2718 (2012).
46. Park, Y.-L. et al. Design and control of a bio-inspired soft wearable robotic device for ankle-foot rehabilitation. *Bioinsp. Biomim.* **9**, 016007 (2014).
47. Cheng, W., Luo, Z., Wang, C., Zhao, T. & Xiang, N. Soft crawling robot integrated with liquid metal-based flexible strain sensor and closed-loop feedback control. *Sens. Actuators A Phys.* **371**, 115316 (2024).
48. Hu, D., Giorgio-Serchi, F., Zhang, S. & Yang, Y. Stretchable e-skin and transformer enable high-resolution morphological reconstruction for soft robots. *Nat. Mach. Intell.* **5**, 261–272 (2023).
49. Shih, B. et al. Electronic skins and machine learning for intelligent soft robots. *Sci. Robot.* **5**, eaaz9239 (2020).
50. Shin, H.-S. & Bergbreiter, S. A modular soft sensing skin for fast measurement of wing deformation in small unmanned aerial vehicles. *Soft Robot.* **11**, 878–888 (2024).
51. Tu, R., Delplanche, R. A., Tobalske, B. W., Inman, D. J. & Sodano, H. A. 3d printed feathers with embedded aerodynamic sensing. *Bioinsp. Biomim.* **19**, 066010 (2024).
52. Qian, L., Ting, T., Benlong, W. & Zhimiao, Y. Avian-inspired embodied perception in biohybrid flapping-wing robotics. *Nat. Commun.* **15**, 9099 (2024).
53. Aracri, S. et al. Soft robots for ocean exploration and offshore operations: a perspective. *Soft Robot.* **8**, 625–639 (2021).
54. Laschi, C. Embodied intelligence in soft robotics: joys and sorrows. *IOP Conf. Ser.: Mater. Sci. Eng.* **1261**, 012002 (2022).
55. Iida, F. & Giardina, F. On the timescales of embodied intelligence for autonomous adaptive systems. *Annu. Rev. Control Robot. Autonom. Syst.* **6**, 95–122 (2023).
56. Kortman, V. G., Mazzolai, B., Sakes, A. & Jovanova, J. Perspectives on intelligence in soft robotics. *Adv. Intell. Syst.* **7**, 2400294 (2025).
57. Micklem, L., Weymouth, G. & Thornton, B. Energy-efficient tunable-stiffness soft robots using second moment of area actuation. In *2022 IEEE/RSJ International Conference on Intelligent Robots and Systems (IROS)*, 5464–5469 (IROS, 2022).
58. Vogel, S. Drag and reconfiguration of broad leaves in high winds. *J. Exp. Bot.* **40**, 941–948 (1989).
59. Hoang, T. T. et al. Soft robotic fabric gripper with gecko adhesion and variable stiffness. *Sens. Actuators A Phys.* **323**, 112673 (2021).
60. Cook, T. et al. Gust estimation and rejection with a disturbance observer for proprioceptive underwater soft morphing wings. In *2026 IEEE International Conference on Robotics and Automation (ICRA)* (ICRA, 2026).

Author contributions

L.M., H.D., Y.Y. and F.G.S. conceived the experiment(s), L.M. and H.D. conducted the experiment(s), L.M. analysed the results, L.M., H.D., Y.Y., G.D.W., and F.G.S. drafted the manuscript and figures, Y.Y., F.G.S., G.D.W., and B.T. provided financial support for the research. All authors reviewed the manuscript.

Competing interests

The authors declare no competing interests.

Additional information

Supplementary information The online version contains supplementary material available at https://doi.org/10.1038/s44182-026-00078-z.

Correspondence and requests for materials should be addressed to Francesco Giorgio-Serchi.